



Thermally-Induced Dopant Segregation Effects on the Space Charge Layer and Ionic Conductivity of Nanocrystalline Gadolinia-Doped Ceria

Jiwoong Bae,^a Yonghyun Lim,^a Jun-Sik Park,^a Dohaeng Lee,^a Soonwook Hong,^a Jihwan An,^b and Young-Beom Kim^{a,c,*}

^aDepartment of Mechanical Convergence Engineering, Hanyang University, Seongdong-gu, Seoul 133-791, Korea

^bManufacturing Systems and Design Engineering (MSDE) Program, Seoul National University of Science and Technology, Nowon-gu, Seoul 139-743, Korea

^cInstitute of Nano Science and Technology, Hanyang University, Seongdong-gu, Seoul 133-791, Korea

Grain boundaries are known to block ionic conduction across grain boundaries in oxide ion conductors due to adjacent space charge layers. Since the positively charged grain boundary core is intensified with a high local concentration of defects such as oxygen vacancies, uniform distribution of a dopant may mitigate the formation of space charge layers and enhance the ionic conductivity. To investigate the dopant segregation effect on the space charge layer and ionic conductivity, we provided thermal energy to nanocrystalline gadolinia-doped ceria (GDC) thin film by post-annealing at different temperatures of 700°C, 900°C, and 1100°C. STEM-EELS analysis demonstrates strong dopant segregation and a higher Ce³⁺ content near the grain boundary than in the bulk after post-annealing. The concurrent segregation of dopants and Ce³⁺ ions implies that once thermal treatment is applied to nanocrystalline GDC thin films, complete space charge layers are formed while the non-thermally treated GDC film with a uniform distribution of dopants has less of a space charge effect and exhibits superior ionic conductivity.
© 2016 The Electrochemical Society. [DOI: 10.1149/2.1201608jes] All rights reserved.

Manuscript submitted May 9, 2016; revised manuscript received June 6, 2016. Published June 15, 2016.

Nanocrystalline materials have attracted a great deal of attention for applications in various energy conversion and storage systems including rechargeable lithium ion batteries, oxygen/ozone gas sensors, oxygen storage systems, and solid oxide fuel cells (SOFCs).¹⁻⁵ Compared to macro- or micro-scale materials, nanocrystalline materials possess extraordinary electrical or electrochemical properties (i.e., ionic conduction or surface exchange reactions). One major cause of the unusual properties is related to the fine grain size (<100 nm), which corresponds to an extremely high grain boundary density. For instance, nanocrystalline calcium oxide-stabilized zirconia (0.14 μm grain size) showed a 15 times higher specific grain boundary conductivity than microcrystalline materials (>4 μm grain size).⁶ In terms of the surface kinetics, a nanocrystalline interlayer (~65 nm grain size) applied to the interface between the cathode and electrolyte of a SOFC exhibited a 5–6 times lower electrode interface resistance than a microcrystalline interlayer (~6 μm grain size).⁷ Therefore, understanding the grain boundary properties is important to appropriately utilize nanocrystalline materials for energy conversion devices due to their exceptional features compared to bulk materials.

Recently, oxide ion conductors (e.g., gadolinia-, samaria-, or yttria-doped ceria (GDC, SDC, or YDC)) usually with a polycrystalline structure, have been widely studied as electrolyte materials for low-temperature SOFCs (LT-SOFCs) since they exhibit higher ionic conductivity and surface exchange rate than the most commonly used electrolyte, yttria-stabilized zirconia (YSZ), especially in the low operating temperature regime (<500°C).⁷⁻⁹ In terms of the ionic conductivity, polycrystalline acceptor-doped ceria has shown grain boundary blocking of ionic conduction originating from the space charge effect.¹⁰⁻¹⁴ A high local concentration of oxygen vacancies near the grain boundary results in a positively charged core. Thereby, oxygen vacancies are depleted near the grain boundary and form space charge layers.¹⁵ As a result of the space charge layers, across the grain boundary resistivity has been reported to be several orders of magnitude higher than the bulk resistivity.¹⁰⁻¹⁴ Therefore, a considerably large volume of grain boundaries is generally anticipated to significantly hinder ionic conduction in nanocrystalline materials.

There have been unexpected studies in which nanocrystalline materials demonstrate similar or even higher ionic conductivities than microcrystalline materials even though the grain boundary densities are considerably higher than microcrystalline densities.¹⁶⁻²¹ The fac-

tors which influence the enhanced ionic conductivity include impurity segregation at the grain boundaries, interface diffusion between the film and the substrate, and overlapping of space charge layers.^{16,17,22} However, even relatively thick (>60 nm thickness) nanocrystalline films with a high purity (>99.9%) and larger grain size (>10 nm) exhibit enhanced ionic conductivities, which has been difficult to explain previously.^{18,19,21} Therefore, if there are no such extrinsic causes, the enhanced ionic conduction may be attributed to intrinsic alteration of the grain boundary properties, primarily attenuated space charge layers.

In this study, we investigated the properties of grain boundaries in nanocrystalline GDC thin films and how they influence the ionic conduction. Thermal energy was purposely provided to nanocrystalline GDC thin films at temperatures from 700°C to 1100°C for dopant redistribution and scanning transmission electron microscopy (STEM) equipped with electron energy loss spectroscopy (EELS) was conducted along with ionic conductivity measurements. Through the spectroscopic and electrochemical analyses, it was demonstrated that thermal treatment causes strong dopant segregation and formation of strong space charge layers while the as-deposited film showed relatively uniform distribution of dopants and attenuated space charge layers, which results in a superior ionic conductivity.

Experimental

Thin film deposition and surface characterizations.—A Gd_{0.2}Ce_{0.8}O_{1.9} ceramic sputtering target (Kurt J. Lesker Company) was used to deposit nanocrystalline GDC thin films with an RF power of 60 W. The substrate was at room temperature which was increased to about 40°C during 4 hrs of deposition. The base pressure was 2 × 10⁻⁶ Torr and the deposition was conducted at 5 mTorr after 30 min of pre-sputtering with the same conditions of deposition under Ar gas flow. The substrate was rotated during the deposition and the sputtering resulted in a deposition rate of about 120 nm/hr. One-sided polished polycrystalline alumina substrates (500 μm thickness, 1 × 1 cm², 99.96% purity, MTI Korea Inc.) were used to deposit the thin films. After deposition, the surface morphology of the nanocrystalline GDC thin films was investigated by FESEM (Nova NanoSEM 450, FEI Corp.) with an acceleration voltage of 15 kV and AFM (XE-70, Park Systems) in the non-contact scanning mode.

TEM-EELS and XPS analysis.—Cross-sectional TEM samples were prepared by an ion milling system (PIPS 691). For the

*Electrochemical Society Member.

[†]E-mail: ybkim@hanyang.ac.kr

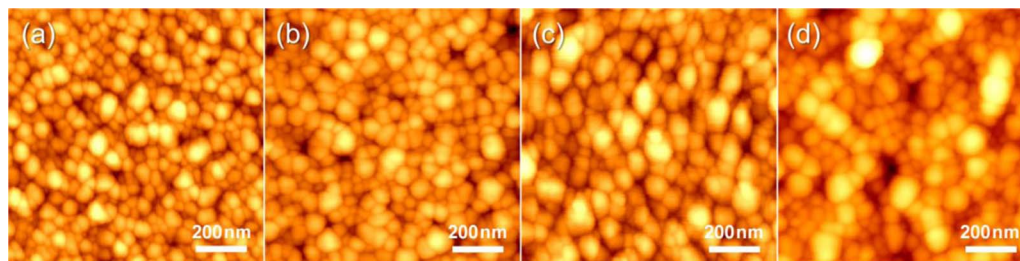


Figure 1. AFM images of nanocrystalline GDC surfaces: (a) as-deposited, (b) 700°C-annealed, (c) 900°C-annealed, and (d) 1100°C-annealed samples.

STEM-EELS analysis, Cs-corrected STEM (JEM-ARM200F, JEOL, USA) was operated at 200 kV. Low-loss EELS was conducted with an interval of 1.1 Å while core-loss EELS was performed with an interval of 2.0 Å for the as-deposited sample and 5.0 Å for the 1100°C-annealed sample. The convergence and collection angles were 8.9 mrad and 20.1 mrad, respectively. The obtained spectra were fitted by MLLS utilizing Digital Micrograph (Gatan Inc.). MLLS fitting is preferred especially for fine-grained combination of two oxide phases since it has better accuracy than intensity integration for compositional studies.^{51–53} The chemical composition and bonding configuration was studied by XPS (Theta probe base system, Thermo Fisher Scientific Co.). The source gun type was Al K α with a spot size of 400 μm^2 and XPS was performed with an energy step size of 1.0 eV (0.05 eV for high resolution) and a constant pass energy of 200 eV. The background of the XPS spectra was subtracted using the Shirley-Sherwood method and then deconvoluted by Gaussian-Lorentzian using XPS peak software.

EIS measurement.—The electrochemical properties were measured using a Gamry Potentiostat (FAS2, Gamry Instruments, Inc.) with nanocrystalline GDC thin films on a polycrystalline alumina substrate after patterning the Pt electrodes. EIS was performed on a tungsten heater with a temperature controller via an in-plane measurement using a two-probe micro-manipulator. The temperature was varied from 350°C to 550°C with a frequency range of 1 MHz to 1 Hz during the measurement. The applied DC biases were 0 V and 0.7 V. The measured EIS data were then fitted to the equivalent circuit model using Gamry Echem Analyst software.

Results and Discussion

Nanocrystalline thin films and grain boundaries.—Nanocrystalline GDC thin films deposited by RF sputtering were post-annealed at 700°C, 900°C, and 1100°C for 10 hrs to systematically provide thermal energy while retaining the nano-granular grains (Fig. 1). Thereby, the morphology of the nanocrystalline thin films exhibited a moderate increase of grain size with increasing annealing temperature. The estimated grain sizes determined from atomic force microscopy (AFM) images are shown in Fig. 2a which are 48 ± 16 nm, 51 ± 16 nm, 62 ± 22 nm, and 66 ± 22 nm for the as-deposited, 700°C-, 900°C-, and 1100°C-annealed samples, respectively. The field emission scanning electron microscopy (FESEM) images in Fig. S1 are in good agreement with the AFM images. This limited grain growth (<100 nm) can be attributed to the moderate annealing temperature ($\leq 1100^\circ\text{C}$) and dopant (Gd^{3+}) addition.^{16,23,24} In addition to the grain size, the grain growth by thermal treatment also causes a decrease of the grain boundary density which was numerically calculated utilizing the AFM images.²⁵ Compared to that of the as-deposited film, the grain boundary density of the films annealed at 700°C, 900°C, and 1100°C gradually decreased by 5.9%, 22.6%, and 27.3%, respectively. However, it should be mentioned that the differences in grain size are negligibly small despite their increase in average grain sizes. Statically speaking, the wide error bars in Fig. 1 and Fig. S1 also indicate that the grain sizes have been almost unchanged due to the moderate annealing temperature. To investigate the crystallinity, X-ray diffraction (XRD) was

performed on nanocrystalline GDC thin films, as shown in Fig. 2b. The as-deposited film has a polycrystalline structure with wide and weak peaks. However, with increasing annealing temperature, GDC (111) becomes stronger at 28° as a sharp and strong peak. It should also be mentioned that after the annealing process at 700°C, all peaks including GDC (111), (200), (220), (311), and (222) appear, indicating a fully-developed crystalline structure.

Figs. 3a–3d shows the cross-sectional and high-resolution TEM images of the as-deposited (Figs. 3a and 3b) and 1100°C-annealed thin films (Figs. 3c and 3d). In Figs. 3a and 3c, both the as-deposited and 1100°C-annealed samples exhibit a columnar structure along the film growth direction (yellow arrows). The white dotted lines in Figs. 3a and 3b indicate the exemplary lines of columnar grain boundaries. The formation of a columnar structure deposited by physical vapor deposition (PVD) methods has also been reported previously.^{26,27} The width of the columns of the 1100°C-annealed sample is slightly larger

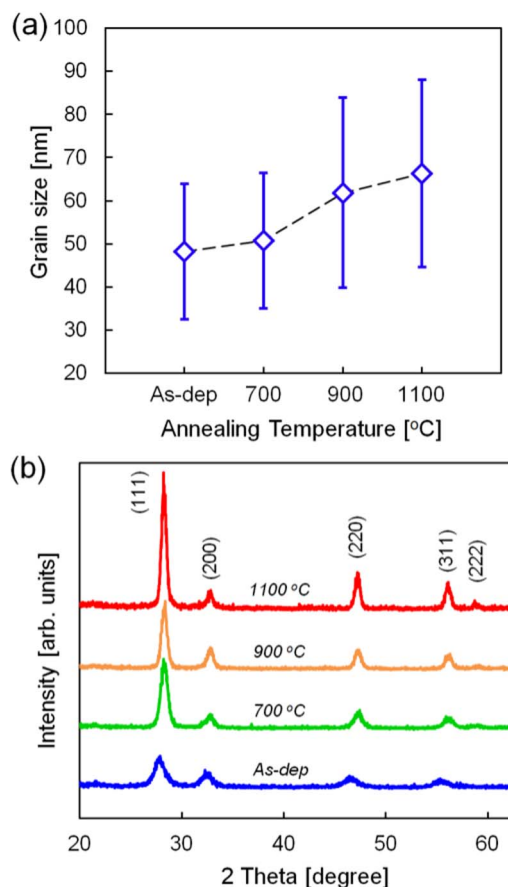


Figure 2. (a) Grain size variation obtained from AFM images and (b) X-ray diffractions of nanocrystalline GDC thin films corresponding to the different annealing temperatures.

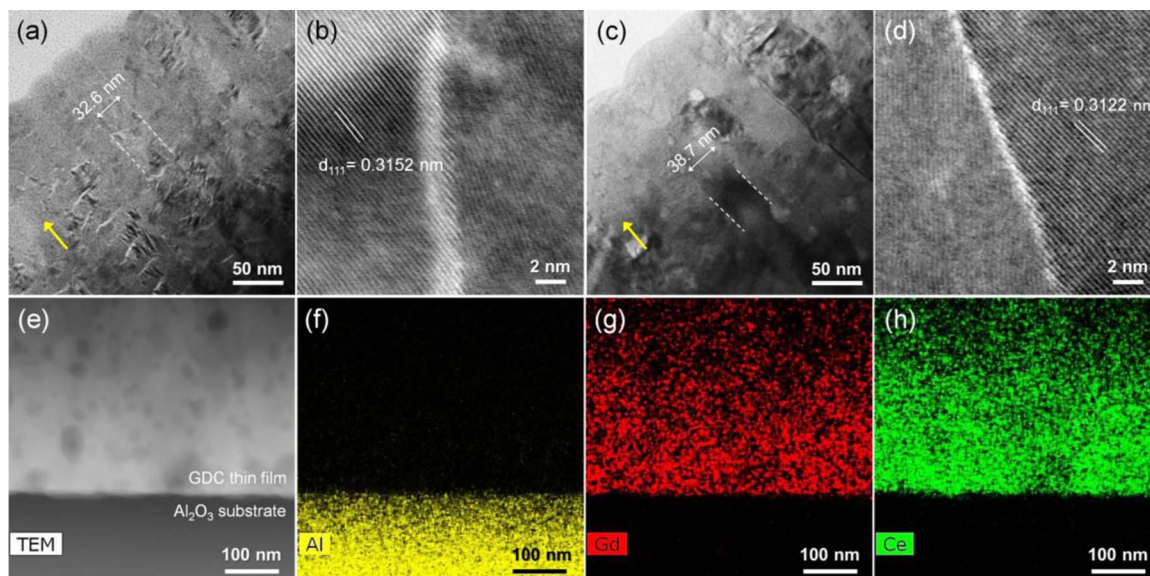


Figure 3. Cross-sectional and high-resolution TEM images of the (a, b) as-deposited and (c, d) 1100°C-annealed nanocrystalline GDC thin films. The yellow lines in (a) and (c) indicate the direction of film growth, and white dotted lines indicate the exemplary lines of grain boundaries. (e) STEM image for TEM-EDS mapping of the 1100°C-annealed sample at the interface between the GDC thin film and polycrystalline alumina substrate for elements of (f) Al, (g) Gd, and (h) Ce.

than that of the as-deposited sample due to grain growth by the thermal treatment. In the high resolution TEM images, the grain boundary structures of the as-deposited (Fig. 3b) and 1100°C-annealed (Fig. 3d) samples were investigated where both images clearly showed tilted grain boundaries. The lattice intervals in the vicinity of the grain boundary measured from the TEM images are 0.3152 nm for the as-deposited sample and 0.3122 nm for the 1100°C-annealed sample. The calculated lattice parameters were 0.5459 nm for the as-deposited sample and 0.5407 nm for the 1100°C-annealed sample. Both values are close to the lattice parameter of ceria (0.5411 nm).^{28–30}

Figs. 3e–3h shows energy dispersive X-ray spectroscopy (EDS) mapping at the interface between the 1100°C-annealed nanocrystalline GDC film and polycrystalline alumina substrate (TEM image is shown in Fig. 3e). Firstly, uniformly distributed Gd and Ce cations can be observed along the film. No local segregation could be detected in these images. In TEM-EDS mapping, it is difficult to determine whether there is a uniform local distribution of cations near the grain boundary or not due to the low resolution. Impurity diffusion (i.e., Al) from the substrate into the nanocrystalline GDC thin film was not present in both the TEM-EDS mapping (Figs. 2f–2h) and XPS data (Al = 0.28 atomic % for the 1100°C-annealed sample).

Dopant distribution near the grain boundary.—It has been widely reported for polycrystalline oxide ion conductors that dopant segregation likely occurs near the grain boundary.^{15,31–35} This dopant segregation strongly influences oxygen nonstoichiometry or vacancy distribution near the grain boundary which alters the ionic properties of nanocrystalline materials.^{31,33,34} Therefore, STEM-EELS was conducted on the as-deposited and 1100°C-annealed nanocrystalline GDC thin films to investigate the thermal effect on the dopant distribution near the grain boundary.

EELS spectra were acquired across the grain boundary with a range of 10 nm and an interval of 1.10 Å, as shown in Fig. 4. The typical Ce $N_{5,4}$ and Gd $N_{5,4}$ -edges of the EELS spectra were obtained after background subtraction. For the as-deposited sample shown in Fig. 4a, Ce $N_{5,4}$ (129 eV) and Gd $N_{5,4}$ edges (150 eV) exhibit a slight reduction near the grain boundary at 0 nm. Fig. 4b shows the EELS spectra of the as-deposited sample extracted from Fig. 4a at the grain interior and boundary for comparison. No significant differences between the spectra obtained at the grain interior and boundary were

observed despite a slight decrease of the grain boundary. This reduced intensity near the grain boundary (in Figs. 4a and 4b) may be due to the loose interfacial atomic structure at the grain boundary.³² However, the intensity area ratios of Gd/Ce are similar at the grain boundary and in the grain interior, implying that the Gd and Ce composition ratio may also be similar. Through the multiple linear least squares (MLLS) fitting of the EELS spectra in Fig. 4a, the dopant distribution was plotted in the range of ± 5 nm from the grain boundary core (Fig. 4c). Firstly, the result shows that the mole fraction at the bulk region estimated from the MLLS fitting is close to that obtained from XPS in Fig. S2 (dotted black lines in Fig. 4c, 12.47 mol%). More importantly, the mole fraction of Gd₂O₃ across the grain boundary is almost unchanged, which indicates random distribution of the dopants.

On the other hand, the EELS spectrum of the 1100°C-annealed sample shows that the Ce $N_{5,4}$ -edge (127 eV) was significantly decreased while the Gd $N_{5,4}$ -edge (148 eV) was slightly increased at the grain boundary (at 5 nm), implying that the ratio of Gd to Ce becomes larger near the grain boundary (Fig. 4d). Each spectrum at the grain interior and boundary demonstrates a clear decrease of the Ce $N_{5,4}$ edge and increase of the Gd $N_{5,4}$ edge (Fig. 4e). Accordingly, the line profile across the grain boundary was plotted through MLLS fitting and exhibits strong dopant segregation near the grain boundary for the 1100°C-annealed sample (Fig. 4f). The segregation half width from the grain boundary core is about 1.2 nm to 1.5 nm, which is similar to the previous experimental and simulation results shown in Table I.^{15,32,33,35} The calculated segregation factor of the average concentration of Gd to Ce was 1.90, which is close to the simulation result of 1.846.¹⁵ However, the segregation factor is much smaller than 2.78 or 2.48 obtained in previous researches, which may be due to the larger volume of grain boundaries for dopants to segregate in addition to the moderate annealing temperatures ($\leq 1100^\circ\text{C}$).^{32,33} Nevertheless, a notable fact is that thermal treatment at a moderate annealing temperature may not cause significant grain growth (Fig. 1), but considerable dopant segregation near the grain boundary (Fig. 4). The additional information of Gd and Ce concentration for both as-deposited and 1100°C-annealed films is shown in Fig. S3.

The different dopant distribution in the as-deposited and 1100°C-annealed films shown in Figs. 4c and 4f influence the chemical composition near the grain boundary as well. In particular, the defect chemistry or oxygen vacancy profile may be affected according to uniform or segregated dopants due to the dopant-vacancy associations. H. Lee

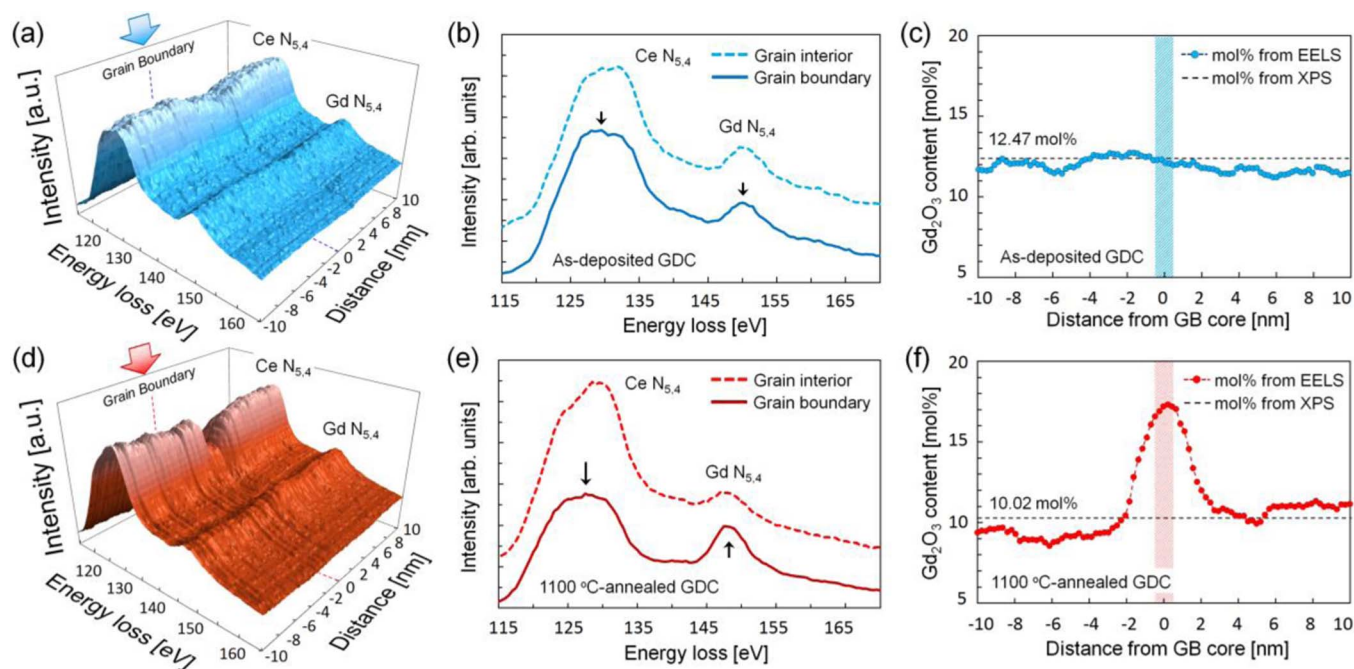


Figure 4. Low-loss EELS spectra with Ce $N_{5,4}$ and Gd $N_{5,4}$ edges (a) across the grain boundary of about 10 nm, (b) at the grain interior and boundary, and (c) the mole fraction, $Gd_2O_3/(Gd_2O_3+CeO_2)$, across the grain boundary for the as-deposited sample. (d-f) Equivalent plots for the 1100°C-annealed sample. (EELS interval = 1.1 Å).

et al. reported simulation results of nanocrystalline GDC in which Gd ions prefer to be associated with oxygen vacancies at the first nearest neighbors (FNN) or second nearest neighbors (SNN).¹⁵ Therefore, Gd segregation also reinforces oxygen vacancy segregation due to this dopant-vacancy association.¹⁵ Considering this correlation between the dopant-vacancy association and segregation, it can be plausibly inferred that oxygen vacancies are also randomly distributed in the as-deposited film while they are segregated near the grain boundary in the 1100°C-annealed film.

Cerium reduction near the grain boundary.—Evidence of different dopant distributions before/after thermal treatment is a significant clue, implying alternation of the vacancy profiles among these films. Therefore, core-loss EELS was conducted to investigate the valence state of Ce in order to evaluate the oxygen vacancy distribution near the grain boundary. In the cubic-fluorite structure of ceria, Ce may have two valence states, Ce^{4+} and Ce^{3+} , depending on the participation of 4f electrons in chemical bonding.^{36–39} This valence state change of Ce also indicates the presence of oxygen vacancies due to the charge neutralization when the electrons are left behind for oxygen vacancy formation.^{33,38,39} In the EELS spectra, the core-loss edge of Ce $M_{5,4}$ has distinct valence-specific shapes, referred to as white line, that is separated in energy and often used to distinguish the valence state of Ce.³⁷ Therefore, further investigation of the Ce valence state was conducted to understand the distribution of Ce^{4+} and Ce^{3+} or oxygen vacancy profiles near the grain boundary.

Fig. 5 shows the core-loss EELS spectra across the grain boundary of about 8 nm with clear white lines of the Ce M_5 and Ce M_4 edges. Fig. 5a shows the core-loss EELS spectra of the as-deposited sample which exhibits a subtle decrease in both the Ce M_5 and Ce M_4 edges near the grain boundary, which was also observed in the low-loss EELS spectra shown in Fig. 4a. In Fig. 5b, two spectra extracted at the grain interior and boundary show clear Ce M_5 and M_4 edges which have maxima at 885 eV and 903 eV, respectively, which are separated by 18 eV. These Ce $M_{5,4}$ edges in the as-deposited sample correspond well to the previously reported $M_{5,4}$ edges of Ce^{4+} in CeO_2 .³⁷ Furthermore, the peak intensity ratio of Ce M_5 to Ce M_4 in both spectra are almost similar, indicating that the valence states of Ce are not very different. In the case of the 1100°C-annealed film shown in Fig. 5c, the Ce M_5 and M_4 edges are significantly reduced near the grain boundary, which is also in good agreement with the low-loss spectrum shown in Fig. 4d. Fig. 5d shows the Ce M_5 and Ce M_4 edges for the 1100°C-annealed sample, which have energy loss maxima at 883 eV and 901 eV, respectively, which are also separated by 18 eV. These maxima are close to the well-known Ce^{3+} $M_{5,4}$ edges in Ce_2O_3 .^{36–38} Notably, the Ce M_4 edge in the grain boundary shows a weaker peak intensity than in the grain interior which indicates that the Ce^{3+} valence is more preferred to Ce^{4+} at the grain boundary. Fig. 5e shows the line profile across the grain boundary with the M_5/M_4 intensity ratio calculated by positive parts of second derivative of the EELS spectra shown in Figs. 5a and 5c. For the as-deposited sample, the M_5/M_4 intensity ratio is close to 0.90, which indicates that Ce^{4+} is preferential.^{30,38} The important result is that the variation of the M_5/M_4 intensity ratio

Table I. Properties of the Grain Boundary in Nanocrystalline GDC.

Annealing temperature	Segregation half width	Segregation factor	Ce M_5/M_4 ratio	Method	Author	Ref. number
650°C	1.5–2.0 nm	1.4	-	Experiment (STEM-EELS)	W. Lee et al.	35
1100°C	1.2–1.5 nm	1.9	1.08–1.20	Experiment (STEM-EELS)	This study	-
1300°C	~2.0 nm	-	0.95–1.20	Experiment (STEM-EELS)	Y. Lin et al.	34
1350°C	1.9–2.5 nm	2.48	-	Experiment (STEM-EELS)	W.J. Bowman et al.	32
1500–1600°C	2.0–2.5 nm	2.78	1.00–1.20	Experiment (STEM-EELS)	Y. Lei et al.	33
1727°C	~1.0 nm	1.846	-	Simulation (MD-MC)	H. Lee et al.	15

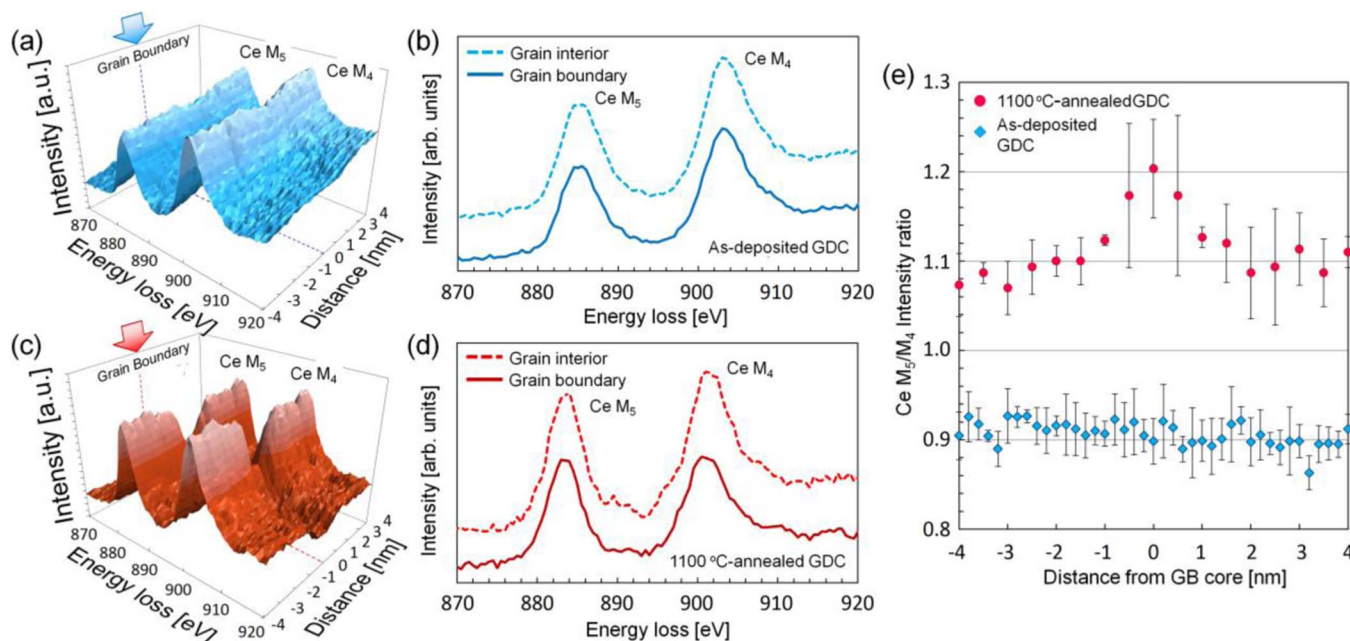


Figure 5. Core-loss EELS spectra with Ce M_5 and M_4 edges (a) across the grain boundary of about 8 nm and (b) at the grain interior and grain boundary for the as-deposited sample. (c, d) The equivalent plots for the 1100°C-annealed sample. (e) The Ce M_5/M_4 intensity ratio across the grain boundary (EELS interval = 2.0 Å for the as-deposited film and 5.0 Å for the 1100°C-annealed film).

is not significant near the grain boundary, which means oxygen vacancies are also randomly distributed across the grain boundary or it is possible that there may be a slight difference which is too small to detect in the EELS measurement. The random distribution of dopants and oxygen vacancies resulted in a stable Ce^{4+} valence state. The intensity ratio of the 1100°C-annealed film shows a large variation from 1.08 (grain interior) to 1.20 (grain boundary), which is similar to previous EELS studies in which Y. Lei et al. reported that the M_5/M_4 intensity ranged from 1.0 to 1.20 and Y. Lin et al. reported similar values in the range of 0.95 to 1.20 (Table I).^{33,34} The increased M_5/M_4 ratio of the annealed sample near the grain boundary implies that the Ce^{3+} concentration significantly increased near the grain boundary, which also indicates oxygen vacancy segregation near the grain boundary. The Ce^{3+} segregation half width is 1.0 nm to 1.5 nm, which coincides with the dopant segregation half width in Fig. 4f, which is 1.2 nm to 1.5 nm. Therefore, it can be inferred that Gd segregation to the grain boundary may influence the Ce valence state including oxygen vacancy profiles near the grain boundary. The slightly higher M_5/M_4 ratio (the average is ~ 1.08) away from the grain boundary core in the 1100°C-annealed sample may be attributed to some ceria reduction due to electron-beam damage experienced during the EELS measurement. The reduction of ceria due to the electron-beam has been previously reported.^{37,40} However, it is clear that the valence states of Ce at the grain interior and at the grain boundary are different, indicating that Ce^{3+} is preferential near the grain boundary.

Further investigation of the Ce valence state at the film surface and interior of the GDC thin films was conducted by evaluating the Ce 3d spectra obtained using X-ray photoelectron spectroscopy (XPS).⁴¹⁻⁴³ Fig. 6a shows the representative XPS spectrum of the as-deposited GDC film at the film interior, which also has deconvoluted lines from the conventional fitting method (see Fig. S4 for the other samples).^{44,45} Among those lines, the spin orbital doublets of (v_0 , u_0) and (v' , u') are the characteristic peaks of Ce^{3+} while all other peaks are those of Ce^{4+} .^{42,45-47} If the intensities of (v_0 , u_0) and (v' , u') are increasing, the concentration of Ce^{3+} among the film increases as well. Through the quantitative analysis, the concentration of Ce^{3+} at the surface and interior of the nanocrystalline GDC thin films was estimated.^{44,45,48} Fig. 6b shows the calculated concentration of Ce^{3+} at the film surface

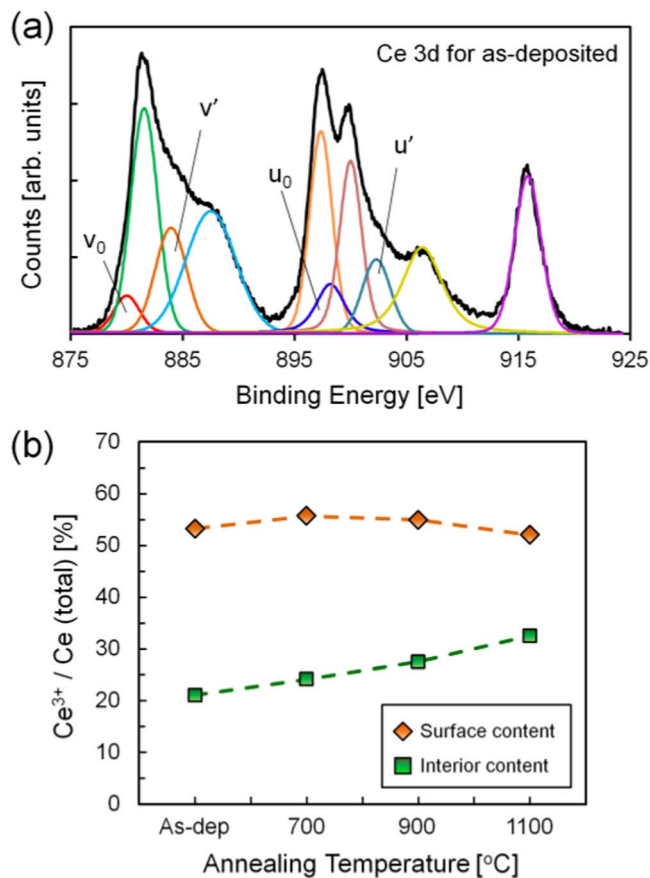


Figure 6. (a) Representative XPS spectrum and deconvoluted peaks at the interior of the as-deposited nanocrystalline GDC thin film. (b) The concentration ratio of Ce^{3+} at the surface and interior of nanocrystalline GDC thin films according to the annealing temperature.

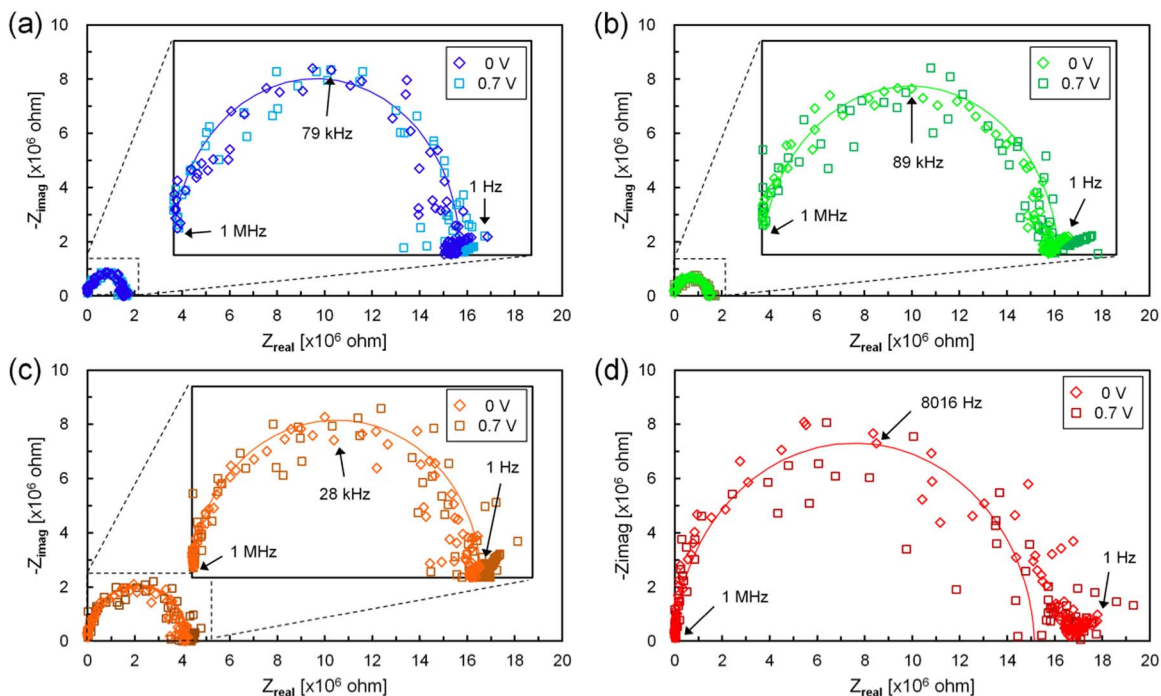


Figure 7. The representative EIS spectra measured at 400°C under different DC biases of 0 V and 0.7 V for the (a) as-deposited, (b) 700°C-annealed, (c) 900°C-annealed, and (d) 1100°C-annealed samples.

and interior according to the different annealing temperatures. For investigation of the film interior, XPS was conducted after 30 sec of Ar etching. This etching process assures that the contribution of the surface segregation of Gd^{3+} , Ce^{3+} , or vacancies, which are accumulated at the free surface when annealing is performed, could be excluded. The Ce^{3+} content shows different behaviors at the film surface and interior. As expected, a high Ce^{3+} content of about 50% was observed at the surface and the variation depending on the annealing temperature was negligibly small. On the other hand, increasing Ce^{3+} content was observed with increasing annealing temperature with values of 21%, 24%, 28%, and 33% for the as-deposited, 700°C-, 900°C-, and 1100°C-annealed samples, respectively. Despite the decreased Ce^{3+} content compared to that of the film surface, this increasing Ce^{3+} concentration in the annealed film also supports the increased M_5/M_4 intensity ratio displayed in Fig. 5c. We speculate that due to dopant segregation, oxygen vacancies are accumulated near the grain boundary and thus, Ce^{3+} ions are newly generated as well. One of the other possible reasons of the increasing Ce^{3+} content is nano-pores which may be generated during the annealing process at a high temperature. As shown in Fig. 3e, the thermal treatment also inevitably generates nano-pores due to grain growth and the free surface of nano-pores may be reduced. Even though the TEM-EELS and XPS results coincide with reduced Ce ions, the fundamental mechanism or driving force of Ce^{3+} generation is not yet defined, which surely needs further investigation to determine the correlation of dopant segregation with defect chemistry.

Electrochemical analysis – ionic conduction in nanocrystalline GDC.—To determine the effect of the grain boundary on the electrical properties of nanocrystalline GDC thin films, electrochemical impedance spectroscopy (EIS) was conducted in the temperature range of 350°C to 550°C at DC biases of 0 V and 0.7 V. Fig. 7 shows the representative Nyquist plots obtained at 400°C, which demonstrate that all samples exhibit one semicircle and one small tail. The high frequency circle is independent of the DC bias, indicating that the semicircle represents ionic conduction through the electrolyte.^{17,26,27} The small tail observed in the low frequency regime is known to result from electrode contribution which is dependent on the DC bias.^{23,49}

The Nyquist plots of as-deposited film at different temperatures are shown in Fig. S5 as a representative. Nonetheless, it was not possible to distinguish the bulk and grain boundary contribution of the electrolyte in the EIS spectra. Due to the relatively thin film (~500 nm) and large electrodes distance (~250 μm), the resistances becomes significantly large, resulting in noises in the spectra. However, due to its extremely high grain boundary densities, we speculate that the EIS circles are mainly due to the grain boundary. It has also been reported by many studies of nanocrystalline oxide ion conductors which usually have an extremely small bulk semicircle while the grain boundary semicircle is dominantly large.^{10,14,32,49,50}

Each representative Nyquist plot is plotted in Fig. 8a for comparison and the smallest circle was observed for the 700°C-annealed film and a slightly larger circle was observed for the as-deposited film. As the annealing temperature increased, the semicircle became larger for the 900°C- and 1100°C-annealed films. For the evaluation of ionic conductivity, the EIS plots were fitted to the equivalent circuit model in the inset of Fig. 8a and then, the ionic conductivity and activation energy are plotted using an Arrhenius relationship in Fig. 8b. First of all, the 700°C-annealed sample exhibits superior conductivity compared to the other samples. We speculate that the enhanced conductivity of the 700°C-annealed film may be due to increased crystallization with annealing at 700°C (Fig. 2b). The 700°C-annealed sample is expected to have the similar grain size and dopant distribution to those of as-deposited sample, while crystalline structure is developed. As a result, we believed that the ionic conductivity of 700°C-annealed sample is slightly increased due to the increased bulk ionic conductivity by enhanced crystallinity. The as-deposited GDC showed a comparable conductivity and slightly lower activation energy ($E_a = 0.86$ eV for the as-deposited sample and $E_a = 0.89$ eV for the 700°C-annealed sample). On the other hand, further increasing the annealing temperature resulted in decreasing total conductivity and increasing activation energy ($E_a = 0.93$ eV for the 900°C-annealed sample and $E_a = 0.95$ eV for the 1100°C-annealed sample). Therefore, for nanocrystalline GDC thin films, increasing the annealing temperature above 700°C may deteriorate the ionic conductivity.

Previous spectroscopic study and electrochemical analysis may imply that the enhanced ionic conductivity of the nanocrystalline thin

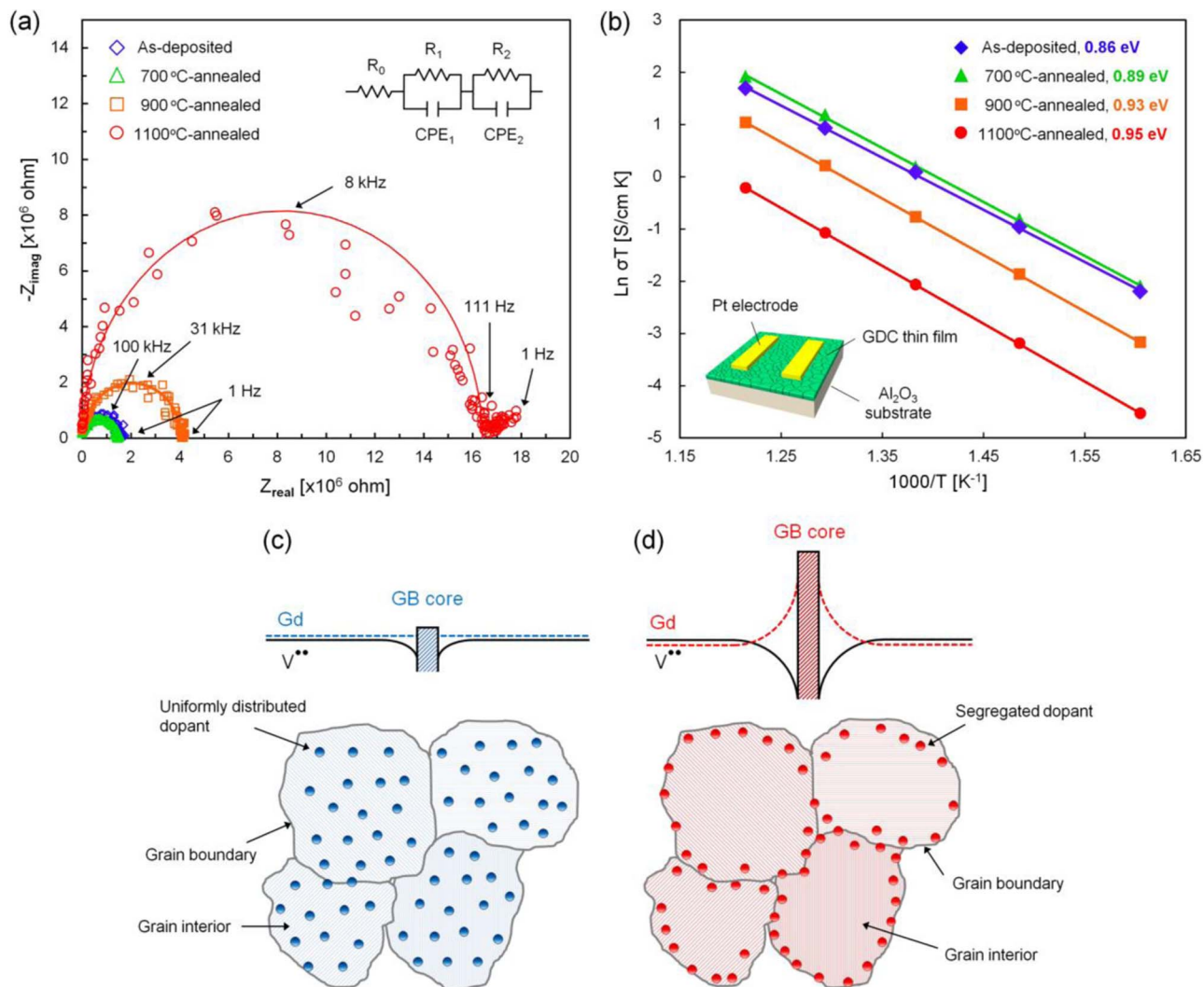


Figure 8. (a) EIS spectra measured at 400°C under a DC bias of 0.7 V with samples annealed at different temperatures (inset shows the equivalent circuit model) and (b) Arrhenius plots of the ionic conductivity and activation energy (inset shows the geometry of ionic conduction measurement). Schematics of the space charge layer estimation and dopant distribution for the (c) as-deposited and (d) post-annealed nanocrystalline GDC grains.

films (as-deposited and 700°C -annealed samples) can be attributed to attenuated space charge layers. A random dopant distribution and Ce valence state were observed across the grain boundary in non-thermally treated (or low annealing temperature, i.e., 700°C) films, which imply that the oxygen vacancies are also randomly distributed in these films (Fig. 4c and Fig. 5e). In other words, the grain boundary core charge is negligibly small, indicating an incomplete electrical grain boundary (not fully developed space charge layers), as depicted in Fig. 8c.¹³ Therefore, the as-deposited and 700°C -annealed thin films with attenuated space charge layers exhibit superior conductivities due to the alleviated grain boundary blocking effect. In the case of the 700°C -annealed film, the conductivity was more enhanced due to crystallization, but still, a moderate annealing temperature may not develop complete space charge layers. On the other hand, once thermal treatment with a sufficiently high annealing temperature for dopant mobility is applied, dopants segregate toward the grain boundary and consequently, the local concentration of oxygen vacancies increases near the grain boundary. Thus, it results in a positively charged core and adjacent space charge layers which significantly lower the overall ionic conductivity (Fig. 8d). Regarding to the crystalline structure, bulk ionic conductivity of 900°C - and 1100°C -annealed samples may be increased by enhanced crystallinity (Fig. 2b). However, once the annealing temperature increases (e.g., $\geq 900^\circ\text{C}$), the well-formed space

charge layer near grain boundaries may dominantly deteriorate ionic conductivity alleviating the increased bulk conductivity.

Similar trends of the enhanced total conductivity in nanocrystalline grains have been observed in previous studies where a low temperature process was applied to fabricate various oxide ionic conductors.¹⁶⁻²¹ Table S1 summarizes the diverse fabrication methods (spray-pyrolysis, pulsed laser deposition (PLD), fast-firing, and atomic layer deposition (ALD)) and conditions employed including the fabrication temperatures. Interestingly, most of the studies fabricated nanocrystalline films under 700°C and then, an annealing process was applied to vary the grain size at higher temperatures. As a result, decreasing total conductivity was also observed with increasing grain size or annealing temperature.¹⁶⁻²¹ It is speculated that these low temperature fabrication methods would suppress the formation of space charge layers while conventional fabrication methods at high temperatures may intensify the space charge zone due to defect segregation. Recent studies regarding co-doping of Gd/Pr or a mixture of GDC+CoFe₂O₄ have reported suppression of dopant segregation which enhances ionic conductivity by increased specific bulk/grain boundary conductivity or mitigated space charge layers.^{32,34} Therefore, when the dopant distribution is uniform, the space charge potential would be lowered and the blocking effect of the grain boundary can be mitigated.

Conclusions

Thermally-induced dopant segregation and the corresponding ionic conduction in nanocrystalline GDC thin films were investigated. Thermal energy was provided via a post-annealing process at 700°C, 900°C, and 1100°C where a slightly increasing grain size was obtained. Through the STEM-EELS analysis, it was found that dopant segregation occurs when thermal treatment is applied while uniform distribution was acquired in the as-deposited thin film. As a result of the homogeneous distribution of dopant, an enhanced ionic conductivity was observed which implies less blocking of grain boundaries by an attenuated space charge layer. On the other hand, the annealed films showed inferior conductivities compared to the as-deposited film due to the complete formation of a space charge layer. The spectroscopic evaluation of the uniform distribution of dopant demonstrated that the space charge layer can be suppressed in the low temperature process resulting in enhanced ionic conductivity. Therefore, the results of this study will provide insight of space charge layer formation and will help in the design of nanocrystalline ionic conductors.

Acknowledgment

Y.B.K. gratefully acknowledges financial support from Technology Advancement Research Program (TARP) funded by Ministry of Land, Infrastructure and Transport of Korean government (grant No. 15CTAP-C078948-02) and the National Research Foundation (NRF) of the Korean Ministry of Education, Science, and Technology (MEST) (grant No. NRF-2015R1A2A1A16074935).

References

- L. Ji, Z. Lin, M. Alcoutlabi, and X. Zhang, *Energy & Environmental Science*, **4**, 2682 (2011).
- V. R. Mastelaro, S. C. Zilio, L. F. da Silva, P. I. Pelissari, M. I. B. Bernardi, J. Guerin, and K. Aguir, *Sensors and Actuators B: Chemical*, **181**, 919 (2013).
- J. Zhang, H. Kumagai, K. Yamamura, S. Ohara, S. Takami, A. Morikawa, H. Shinjoh, K. Kaneko, T. Adschiri, and A. Suda, *Nano Lett.*, **11**, 361 (2011).
- E. Mamontov, T. Egami, R. Brezny, M. Koranne, and S. Tyagi, *J. Phys. Chem. B*, **104**, 11110 (2000).
- S. J. Litzelman, J. L. Hertz, W. Jung, and H. L. Tuller, *Fuel Cells*, **8**, 294 (2008).
- M. Aoki, Y.-M. Chiang, I. Kosacki, L. J.-R. Lee, H. Tuller, and Y. Liu, *J. Am. Ceram. Soc.*, **79**, 1169 (1996).
- Y. B. Kim, J. H. Shim, T. M. Gür, and F. B. Prinz, *J. Electrochem. Soc.*, **158**, B1453 (2011).
- H. Inaba and H. Tagawa, *Solid State Ionics*, **83**, 1 (1996).
- J. Bae, S. Hong, B. Koo, J. An, F. B. Prinz, and Y.-B. Kim, *J. Eur. Ceram. Soc.*, **34**, 3763 (2014).
- S. Kim and J. Maier, *J. Electrochem. Soc.*, **149**, J73 (2002).
- X. Guo, W. Sigle, and J. Maier, *J. Am. Ceram. Soc.*, **86**, 77 (2003).
- X. Guo, *Scr. Mater.*, **65**, 96 (2011).
- X. Guo and R. Waser, *Prog. Mater. Sci.*, **51**, 151 (2006).
- H. L. Tuller, *Solid State Ionics*, **131**, 143 (2000).
- H. B. Lee, F. B. Prinz, and W. Cai, *Acta Mater.*, **61**, 3872 (2013).
- T. Suzuki, I. Kosacki, and H. U. Anderson, *Solid State Ionics*, **151**, 111 (2002).
- I. Kosacki, C. Rouleau, P. Becher, J. Bentley, and D. Lowndes, *Solid State Ionics*, **176**, 1319 (2005).
- M. G. Bellino, D. G. Lamas, and N. E. Walsõe de Reça, *Adv. Funct. Mater.*, **16**, 107 (2006).
- J. L. M. Rupp and L. J. Gauckler, *Solid State Ionics*, **177**, 2513 (2006).
- J. H. Shim, C.-C. Chao, H. Huang, and F. B. Prinz, *Chem. Mater.*, **19**, 3850 (2007).
- J. An, J. Bae, S. Hong, B. Koo, Y.-B. Kim, T. M. Gür, and F. B. Prinz, *Scr. Mater.*, **104**, 45 (2015).
- N. Sata, K. Eberman, K. Eberl, and J. Maier, *Nature*, **408**, 946 (2000).
- K.-R. Lee, J.-H. Lee, and H.-I. Yoo, *J. Eur. Ceram. Soc.*, **34**, 2363 (2014).
- J. L. M. Rupp, A. Infantina, and L. J. Gauckler, *Acta Mater.*, **54**, 1721 (2006).
- M. Miyayama and H. Yanagida, *J. Am. Ceram. Soc.*, **67**, C-194 (1984).
- Y. B. Kim, T. M. Gür, H.-J. Jung, S. Kang, R. Sinclair, and F. B. Prinz, *Solid State Ionics*, **198**, 39 (2011).
- S. W. Kim, Y. Lee, and G. M. Choi, *Solid State Ionics*, **262**, 411 (2014).
- H.-W. Chiang, R. N. Blumenthal, and R. A. Fournelle, *Solid State Ionics*, **66**, 85 (1993).
- B. C. H. Steele, K. M. Hori, and S. Uchino, *Solid State Ionics*, **135**, 445 (2000).
- B. Wang, R. J. Lewis, and A. N. Cormack, *Acta Mater.*, **59**, 2035 (2011).
- J. An, J. S. Park, A. L. Koh, H. B. Lee, H. J. Jung, J. Schoonman, R. Sinclair, T. M. Gur, and F. B. Prinz, *Sci. Rep.*, **3**, 2680 (2013).
- W. J. Bowman, J. Zhu, R. Sharma, and P. A. Crozier, *Solid State Ionics*, **272**, 9 (2015).
- Y. Lei, Y. Ito, N. D. Browning, and T. J. Mazanec, *J. Am. Ceram. Soc.*, **85**, 2359 (2002).
- Y. Lin, S. Fang, D. Su, K. S. Brinkman, and F. Chen, *Nat. Commun.*, **6**, 6824 (2015).
- W. Lee, H. J. Jung, M. H. Lee, Y.-B. Kim, J. S. Park, R. Sinclair, and F. B. Prinz, *Adv. Funct. Mater.*, **22**, 965 (2012).
- J. A. Fortner, E. C. Buck, A. J. G. Ellison, and J. K. Bates, *Ultramicroscopy*, **67**, 77 (1997).
- L. A. J. Garvie and P. R. Buseck, *J. Phys. Chem. Solids*, **60**, 1943 (1999).
- H. Hojo, T. Mizoguchi, H. Ohta, S. D. Findlay, N. Shibata, T. Yamamoto, and Y. Ikuhara, *Nano Lett.*, **10**, 4668 (2010).
- Z.-P. Li, T. Mori, F. Ye, D. Ou, G. J. A. Aachterlonie, J. Zou, and J. Drennan, *J. Phys. Chem. C*, **116**, 5435 (2012).
- D.-B. Katherine, K. Haruo, Y. Katsuhiko, H. Teruhisa, and Y. Harumi, *Nanotechnology*, **26**, 215401 (2015).
- J. P. Holgado, G. Munuera, J. P. Espinós, and A. R. González-Elipe, *Appl. Surf. Sci.*, **158**, 164 (2000).
- M. V. Rama Rao and T. Shripathi, *J. Electron Spectrosc. Relat. Phenom.*, **87**, 121 (1997).
- M. Romeo, K. Bak, J. El Fallah, F. Le Normand, and L. Hilaire, *Surf. Interface Anal.*, **20**, 508 (1993).
- S. Deshpande, S. Patil, S. V. Kuchibhatla, and S. Seal, *Appl. Phys. Lett.*, **87**, 133113 (2005).
- P. Hartmann, T. Brezesinski, J. Sann, A. Lotnyk, J.-P. Eufinger, L. Kienle, and J. Janek, *ACS Nano*, **7**, 2999 (2013).
- Y.-L. Kuo, C. Lee, Y.-S. Chen, and H. Liang, *Solid State Ionics*, **180**, 1421 (2009).
- Y.-L. Kuo, Y.-S. Chen, and C. Lee, *J. Eur. Ceram. Soc.*, **31**, 3127 (2011).
- C. Korsvik, S. Patil, S. Seal, and W. T. Self, *Chem. Commun.*, 1056 (2007).
- X. Guo and J. Maier, *J. Electrochem. Soc.*, **148**, E121 (2001).
- H. J. Avila-Paredes, K. Choi, C.-T. Chen, and S. Kim, *J. Mater. Chem.*, **19**, 4837 (2009).
- C. Colliex, *J. Electron. Microsc.*, **45**, 44 (1996).
- Y. Pan, A. Brown, R. Brydson, A. Warley, A. Li, and J. Powell, *Micron*, **37**, 403 (2006).
- S. Yakovlev and M. Libera, *Micron*, **39**, 734 (2008).